Research Article Vol. 32, No. 20 / 23 Sep 2024 / *Optics Express* 35331

Optics EXPRESS

Nanowire-based artificial photoreceptors with multi-hyperuniformity inspired by chicken retina

MI JIN HONG,[1,†] MIN JU KIM,[1,†] SU BO LEE,[1] YOUNG MIN SONG,[2,3] AND GIL JU LEE[1,4]

[1] *School of Electrical and Electronics Engineering, Pusan National University, 2, Busandaehak-ro 63 beon-gil, Geumjeong-gu, Busan 46241, Republic of Korea*
[2] *School of Electrical Engineering and Computer Science, Gwangju Institute of Science and Technology, Gwangju 61005, Republic of Korea*
[3] *ymsong81@gmail.com*
[4] *gjlee0414@pusan.ac.kr*
[†] These authors contributed equally to this work.

Abstract: Retinal cells of chicken possess a hyperuniform distribution enabling exceptional spatial sampling. Recently, interest has grown in mimicking biological imaging systems for optoelectronics technology. However, since biological retinal cells and current imaging pixels have a significant scale mismatch such as super-micron and sub-micron, the applicability of hyperuniform distribution must be investigated at sub-micron scale, considering wave-optics phenomena. In this study, we present theoretical analyses and design strategies for nanowire-based artificial photoreceptors with hyperuniformity. Full-wave analyses reveal that the selectivity of hyperuniformly patterned photoreceptors outperforms other configurations for each wavelength (red, green, blue, and near-infrared lights) without additional spectral filters.

1. Introduction

As development progresses in various fields such as robotics, unmanned aerial vehicles, and micro-aerial vehicles progresses, the demand for high-quality imaging systems increases [1–5]. Specifically, a miniaturized wide field of view camera is suggested by mimicking the hemispherical retina and monocentric lens of cichlid [6]. An amphibious artificial vision system is proposed by inspiring the compound eyes of a fiddler crab, overcoming limitations in environmental adaptability [7]. Additionally, emulating cuttlefish eyes provides a hardware solution for dynamic range issues in autonomous driving [8]. Furthermore, avian deep foveae are inspired for identifying colored objects and detecting objects [9]. These works focused on the renovation of the imaging system configurations, such as the features of lenses, the curved image sensors, and the shape of pupil. In addition to these structural improvements, image pixels need to be scaled down to meet the requirement for higher resolution [10–13]. Usually, biological retina cells are predominantly arranged in a highly ordered state (i.e., crystalline). For instance, the light-sensing ommatidia in the compound eye of insects are distributed in a hexagonal pattern [14]. Additionally, the photoreceptors in teleost fish, mantis shrimp, shore crab, and crayfish are arranged in crystalline array [15–19]. Such regularly arranged cone cells enable highly precise recognition and enhance visual capabilities [20–22]. However, a regular arrangement has real space constraints that hinder device compactness with exceptional photon selectivity as reported [23–25]. Maintaining physical tolerance is crucial for the production yields of optical systems as it reduces sensitivity to errors in the fabrication process. To achieve both sensitive detection and beneficial for spatial organization, a more adaptable arrangement of photoreceptors is required.

Among biological entities, avians possess the most sophisticated retina in nature, consisting of various types of cone cells [26–29]. Especially, *Gallus gallus* (i.e., chicken) retina includes five different cone types, including four single cones (i.e., red, green, blue, and violet) for color

#537955 https://doi.org/10.1364/OE.537955
Journal © 2024 Received 30 Jul 2024; revised 24 Aug 2024; accepted 6 Sep 2024; published 16 Sep 2024

detection and double cones to sense light luminance [30]. Each cell type in multicomponent system exhibits outstanding sensitivity to distinct wavelengths within the visible range. Additionally, the cone cell in the chicken retinal photoreceptor can be separated into three main components: the ellipsoid, oil droplet, and outer segment [31,32]. The ellipsoid acts as a waveguide, resulting in lower light loss, while the oil droplets serve as spectral filters, selectively transmitting specific wavelengths. The outer segment is a phototransduction component of the cone cell, which transfers signals to inner segments. Trials to model outer segments in chicken cone cell have been activated in recent studies [33,34], since the outer segment can control the directionality from a layered scattering model. The outer segment also has spatial field distributions according to incident wavelengths. Notably, the arrangement of photoreceptors in the avian retina forms a unique pattern called hyperuniform disordered (HUD), which enhances spatial sampling capability of color and luminance [35]. Hyperuniformity indicates the distribution of points that appear irregular at small scales due to large density fluctuations, which simultaneously exhibits a uniform arrangement resulting from low density fluctuations at large scales [36,37]. This characteristic offers better fabrication tolerance compared to crystalline distribution. Multi-hyperuniformity, a property adhering to the principles of hyperuniformity between different cell types [38], ensures that patterns remain hyperuniform even when some cell types are absent in a multi-HUD array. Furthermore, the HUD structure allows for increased component density per unit chip area and improved device compactness, as it maintains specific distance conditions between adjacent elements [39,40]. In contrast, perfect crystalline arrangements have constraints in achieving packing density beyond a certain threshold due to their fixed lattice pattern.

Despite the advantages of HUD such as photon sensitivity, spatial flexibility, and high packing density, nanoscale HUD systems for spatial light sampling adaptable to a visible image sensor have not yet been explored. Since the pixel pitch of image sensors in contemporary technology approaches the scale of visible wavelengths, an investigation of nanoscale HUD systems is necessary. Therefore, a numerical investigation is required to determine whether HUD stands out in the wave-optics region, which is significantly smaller than the realistic scale of chicken retinal cone cells. Chicken cone cells have distances of 11.4, 10.6, 13.0, 14.5, and 7.5 µm for red, green, blue, violet, and double types, respectively [41]. We decide to use a GaAs nanowire array (NWA) because GaAs has a direct bandgap allowing electrons to transition directly without a change in momentum, whereas silicon and germanium have an indirect bandgap [42,43]. Moreover, GaAs exhibits strong light-matter interaction across a wide range from ultraviolet (UV) to near-infrared (NIR) depending on material composition. By proposing GaAs NWA in HUD pattern, we can classify that the functional effects of the HUD array at the microscale are also effective at the nanoscale, making it applicable for advanced optoelectronics.

In this work, we propose artificial photoreceptors with GaAs NWA arranged in a multi-HUD structure, which benefits from the high photoresponsivity of GaAs and advantages of the hyperuniformity [44,45]. The hyperuniformity in GaAs NWA enhances the narrowband absorption while minimizing optical crosstalk. For designing optimal photoreceptors, the nanowire-based HUD system is optimized in terms of diameter and density. The NWA induces diameter-dependent absorption and affects the HE mode in adjacent nanowires. Therefore, we investigate whether the HE_{11} mode, corresponding to the fundamental mode in the circular structure, predominantly occurs in different types of GaAs NWs. To determine the properly dense HUD array, the HUD arrangement is generated using the Poisson disc packing (PDP) method, followed by efficiency validation via the finite-difference time-domain (FDTD) method. Furthermore, we confirm that the multi-HUD arrangement exhibits the highest resolution compared to regular and random patterns with identical density, specifically revealing the locational advantages. Also, two cases (i.e., GaAs NWs on GaAs substrate and embedded in a PDMS layer) are presented to consider the fabrication process and show wavelength-selective absorption [46,47]. In addition to GaAs, we demonstrate that a Si NWA with multi-HUD arrangements effectively contributes to selective photon absorption, where the right half width at half maximum (HWHM) of absorption efficiency is narrower than that of GaAs. Moreover, in addition to high wavelength selectivity, the HUD arrangement exhibits increased selectivity for polarization when the circular NWA is changed to an elliptical NWA. In summary, we suggest a rigorous optical solution for spatial sampling of light by introducing multi-spectral artificial photoreceptors. Our proposed structure, mimicking the biological visual system, can independently operate without the need for spectral filters such as dyes. Therefore, this novel HUD system perfectly aligns with the future direction of image sensors which aim to perform without color filters. The spatially optimized photoreceptors will shed light on the development of bio-inspired light-sensitive imaging devices.

2. Method

2.1. *Poisson disc packing (PDP) method*

Poisson disc packing is adopted for generation of the HUD points pattern. This is the packing method that scatters a set of points in the two-dimensional Euclidean space where distributed points in close have a specified distance, while covering the entire space as uniformly as possible. We utilize the PDP algorithm based on a previous study [48]. After randomly determining a reference point in space, a new point is generated at a distance between r (i.e., the inner radius) and $2r$ (i.e., the outer radius) from the reference point, where r is the minimum conditional distance between points. These generated points must maintain a minimum distance from all existing points and remain within the specified dimensions. If the generated point does not meet these conditions, it is removed. New points are formed iteratively, adhering to these conditions. This algorithm enables the creation of a pseudo-randomly distributed point set.

2.2. *Optical simulation*

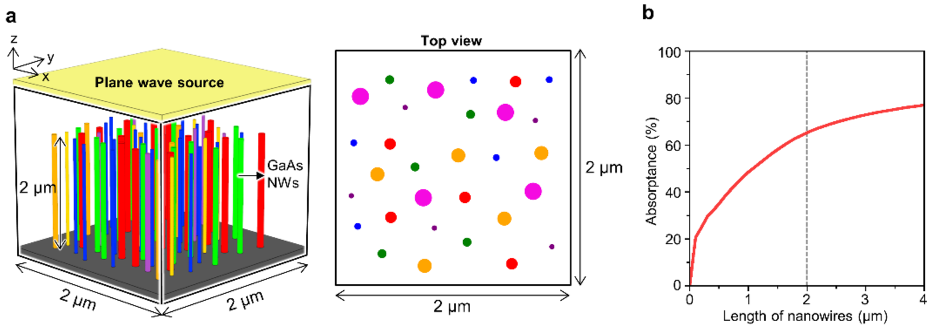

Fig. 1. The simulation domain and absorptance result for increasing the length of nanowires. (a) Simulation domain for implementing the computational study. The simulation domain is set to $2 \times 2\ \mu m^2$ where the GaAs NWA has a fixed length of 2 μm. (b) The absorptance result of the multi-hyperuniform distributed GaAs nanowire array with increasing length of the nanowire.

To demonstrate the optical performances of HUD photoreceptors, we employ a computational study based on FDTD simulation, as shown in Fig. 1(a). FullWAVE (RSoft Design Group, Synopsys, United States) reveals three-dimensional absorption profile and optical efficiencies in the HUD systems with FDTD simulation. The simulation domain is fixed to $2 \times 2\ \mu m^2$, where the GaAs NWA has a fixed length of 2 μm. The 2 μm-long nanowire is appropriate to observe wavelength selectivity as displayed in Fig. 1(b). The grid size for simulation was $5 \times 5 \times 10$ nm (i.e., x, y, and z directions). For HUD and random arrangements, a perfectly matched layer (PML) was applied in all three directions as the simulation boundary conditions. In contrast, for regular arrangement, the boundary conditions were established as periodic in the x- and y- directions and as a PML in the z-direction. After calculation, average results from each polarization are used to consider the intermediate value of transverse electric (TE) mode and transverse magnetic (TM) mode. Furthermore, data visualization is performed by OriginPro 2022 (OriginLab Co., United States) and Python plotting library Matplotlib.

3. Results and discussion

3.1. Generation and estimation process of the multi-hyperuniform pattern

As one of avians, chicken has the sophisticated retinal system with diverse functional tissues such as lens, iris, cornea, sclera, pecten, and retina (Fig. 2(a)). The magnified schematic shows that chicken retina consists of multiple cones which selectively absorb the incident light at broad band of UV to NIR region. The wavelength-selective absorption can occur in the retinal cell array of chicken due to structural parameters and arrangement of photoreceptors. Therefore, both sensitive (i.e., high absorptivity) and selective absorption enable precise recognition for survival. In addition to coloration-perceptive cells, the cone arrangements involve an achromatic cone, which detects the brightness and contrast of an image. Achromatic cones mainly perceive white and black images in low-light environments unlike other cone cells. However, for the application of image sensors, we reconstruct photoreceptors to include six cone cell types according to wavelengths of 380, 465, 532, 630, 750, and 850 nm. Furthermore, our GaAs NW artificial photoreceptors are much simpler form than those in the chicken retina. As shown in Fig. 2(b), a cone cell in the chicken retinal photoreceptor consists of an ellipsoid, oil droplet, and outer segment [31,32]. The ellipsoid functions as a waveguide, minimizing light loss and enhancing transmittance. The oil droplets serve as spectral filters that selectively transmit specific wavelengths while also acting as light-focusing lenses. The outer segment is densely packed with membrane discs containing photopigments, where phototransduction occurs, transferring visual signals. In contrast, GaAs NWs integrate the optical functions of the ellipsoid and oil droplet. With high quantum efficiency, GaAs NWs effectively convert absorbed photons into electron-hole pairs, resulting in a high photocurrent. These NWs also allow electromagnetic waves to be guided within the NW, similar to the waveguiding properties of an ellipsoid, and ultimately absorbed by the NW. Additionally, the NWs exhibit diameter-dependent resonance, selectively absorbing specific wavelengths and directly converting them into current, thereby eliminating the need to mimic the phototransduction function of the outer segment.

To generate a HUD arrangement, the PDP algorithm is utilized. The PDP method distributes points in a two-dimensional Euclidean space, maintaining a specified minimum distance between adjacent points while uniformly covering the space. The detailed process of the PDP method is explained in the “Methods” Section. After a pattern is generated using the PDP method, the generated pattern is evaluated to determine if it is a HUD arrangement through the definition of HUD as given in Eq. (1) [38]:

$$\lim_{k\to 0} S(k) = 0 \tag{1}$$

where S(k) is the structure factor, quantifying how fluctuations spatially distribute and providing insights into dynamics of particles within the system. We can classify a pattern as being arranged in HUD when S(k) converges to zero in the limit as k (i.e., wave vector) approaches zero, as displayed along the red-dashed line (Fig. 2(c)). For a finite point configuration, the structure factor is expressed as Eq. (2):

$$\mathrm{S}(\mathbf{k}) = \frac{1}{N}\left|\sum\nolimits_{j=1}^{N} \exp(i\boldsymbol{k}\cdot\boldsymbol{r}_j)\right|^2 \tag{2}$$

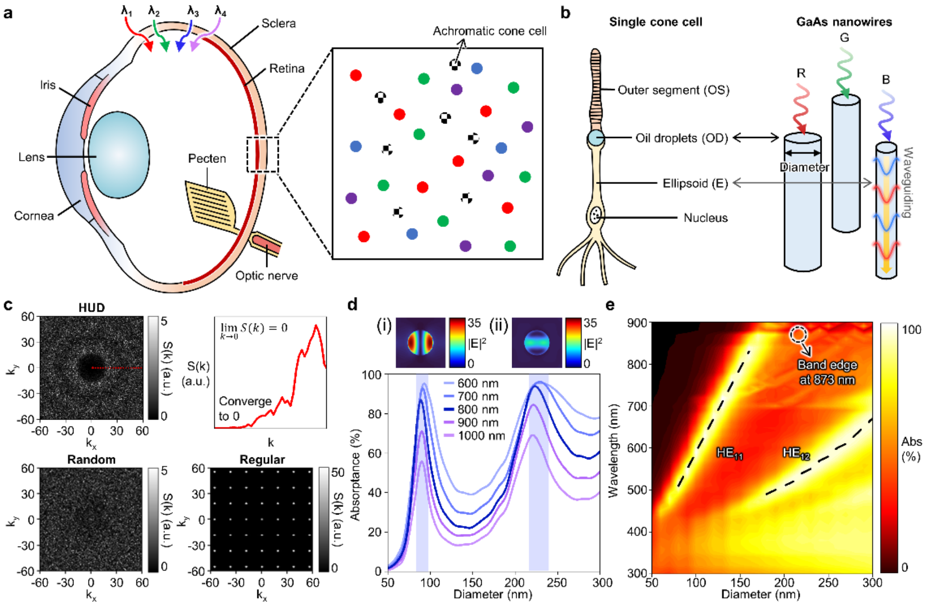

Fig. 2. The hyperuniformity observed in avian eyes and the diameter optimization process for a multi-hyperuniform GaAs nanowire array (NWA). (a) Schematic of the chicken retina, as one example of avian eyes. The chicken eye consists of the lens, iris, cornea, sclera, pecten, and retina. The expanded view shows the various types of cone cells with hyperuniform disordered (HUD) configuration. Cone cells with red, blue, green, and violet types contribute to color detection, while achromatic cone cells detect light luminance. (b) A schematic of a single cone cell in the chicken retina and corresponding functions of a GaAs nanowire. (c) Structure factors (i.e., S(k)) in HUD, random, and regular configuration. In the HUD configuration, we can observe that the S(k) converges to zero as the wave vector, k, approaches zero, indicating that the points arrangement follows the hyperuniform rule. Contrary to the HUD points pattern, the S(k) from the spatial vectors of k_x and k_y has a random distribution in the random configuration, whereas the S(k) emerges as discrete in the regular configurations which include square pattern. (d) The absorptance results for varying the period between same type nanowires from 600 nm to 1000 nm, specifically at a wavelength of 550 nm. i) The electric field density profile indicates that the penetrated electric field is dominant in the 89 nm diameter nanowire. ii) The electric field density profile for the 223 nm diameter nanowire exhibits a weak electric field within the nanowire. (e) At a period of 800 nm, the HE_{11} mode transition occurs according to the increment of the diameter. Therefore, we set the diameters of GaAs NWA to 50, 65, 80, 110, 135, and 165 nm for corresponding wavelengths of 380, 465, 532, 630, 750, and 850 nm, respectively.

where $\boldsymbol{r}$ is the positions of the points, N is the total number of points in the system and $\boldsymbol{k}$ is not included when its value is zero. For two-dimensional space, the wave vector can be obtained as $\boldsymbol{k} = (2\pi n_x/L_x\ ,\ \ 2\pi n_y/L_y)$, where $n = 0, 1, 2, \cdots$ and L is the size of the system. Furthermore, we validate the structure factors for regular and random arrangements, as shown in Fig. 2(c). In contrast to the HUF points pattern, the S(k) from the spatial vectors of k_x and k_y appears randomly distributed in the random configuration, while it emerges as discrete in regular configuration, which is the square pattern.

For optimization of the diameter, period for same type of NWs is previously optimized to emphasize HE_{11} mode, consistent to fundamental mode in a circular waveguide. As the period increases, the fundamental mode becomes narrower with minimum crosstalk, as arranged in Section 1 of Supplement 1. Also, the absorptance at 550 nm over various periods is plotted in

Fig. 2(d). To confirm the optimum point between photon sensitivity and device compactness, we need to find the optimal distance between the same type of NWs. A dense NWA can induce optical crosstalk, while increasing the distance between NWs results in the arrangement being less favorable in terms of compactness. Thereby, the diameter of GaAs NWA is optimized with a period of 700 nm. The above contour maps indicate the electric field density in a single nanowire. Each nanowire has diameter of 89 and 223 nm, which are matched from the blue-colored area. We can observe that the penetrated electric field is intensive in the smaller nanowire where the HE_{11} mode is dominant (Fig. 2(d)(i)). On the other hand, the nanowire with a diameter of 223 nm exhibits a weak electric field within the nanowire (Fig. 2(d)(ii)). As represented in Fig. 2(e), the concentrative electromagnetic field within the nanowire is dominant at specific radius points along the dashed line. Based on simulation results, the diameter of GaAs NWA is decided to 165 (NIR1), 135 (NIR2), 110 (R), 85 (G), 65 (B), and 50 nm (V) corresponding to the wavelengths of 850 nm, 750 nm, 630 nm, 532 nm, 465 nm, and 380 nm, respectively. Discrete peaks at 873 nm exist owing to photonic band edge of GaAs.

3.2. Comparison optical performances dependent on number density

After generation of HUD points, the radial distribution function (RDF) examines the reliability of multi-optical channels (Fig. 3(a)). The RDF is one of molecular dynamics, known as an efficient method for analyzing the interaction of quantum dot ensembles. The probability of a particle being located at a certain distance (r) away from a reference particle can be calculated by the RDF. The RDF measures the average density of particles in a spherical shell of thickness (dr) at distance r from the reference particle. As a function of the distance, the square value of the pair correlation function (i.e., g_2R) is plotted in Fig. 3(b). Individual cone cells and overall population display the convergence in the green/blue-colored region, respectively. From the expanded view, we can demonstrate that same types of NWs maintain the minimum distance of 700 nm. On the other side, the overall population, which is blended with six different types of channels, features a gap of 300 nm between each nanowire. Furthermore, we need to confirm the minimal distance between each cone cell type. As shown in Fig. 3(c), the two-dimensional electric field and absorption profiles present the reasonable distance to minimize optical crosstalk. To consider both the selective absorption and space availability, the condition of minimum distance is essential. The diameters of two nanowires are 135 nm (D_1) and 165 nm (D_2). When the distance between the two nanowires is 300 nm, the smaller nanowire mainly reacts with wavelength at 750 nm, while the larger nanowire responds to the electromagnetic wave at 850 nm.

Next, we find the optimal density of HUD pattern by varying density from 2.8% to 18.3%. Within the fixed simulation domain, each cell type is uniformly scattered in equal quantities across all densities (i.e., the number of each cell type at 7.0% is five). Figure 3(d) exhibits the cumulative sum values of absorption along the z-direction. Two-dimensional absorption profiles visualize the sampling ability of different types of photoreceptors. To numerically compare the selectivity in multiple densities, the absorption efficiency (AE) is induced, which divides the absorption of each type at corresponding wavelength by the total absorption of all types. The optimal density is 7.0% as it exhibits the highest selectivity compared to the other densities (Fig. 3(e)). The equation for AE is shown on the graph. Cases with density over 7.0% have crowded nanowires that generate optical crosstalk from coupling mode and leaky mode. Furthermore, the GaAs HUD structure is attached with a GaAs substrate or transparent polymer (i.e., Polydimethylsiloxane; PDMS) to consider the fabrication process. Figure 3(f) indicates that the absorption of the R type is higher than that of other types, with all cases having a density of 7.0%.

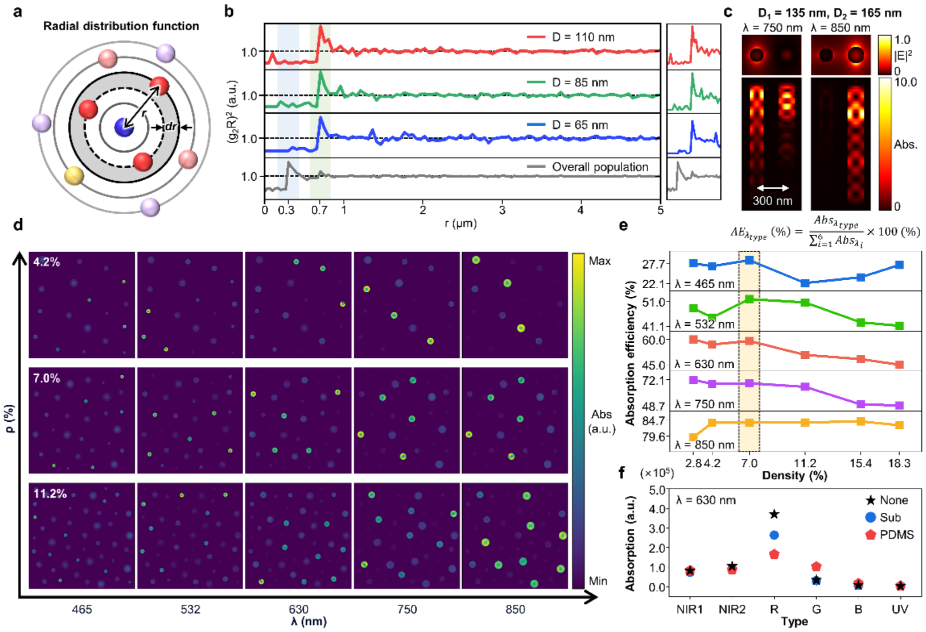

Fig. 3. Density optimization with a multi-HUD arrangement. (a) Validation of the reliability of multi-optical channels using radial distribution function analysis. (b) The squared pair correlation function is shown for individual cone cells and the overall population. The green region at 700 nm indicates individual cell convergence, while the blue region at 300 nm represents overall population convergence. (c) The 2D electric field and absorption profiles indicate an optimal 300 nm distance between nanowires to minimize optical crosstalk. (d) The cumulative absorption values along the z-axis are presented for 4.2%, 7.0%, and 11.2%. The two-dimensional absorption profiles demonstrate the sampling capabilities of different photoreceptor types. (e) The absorption efficiency (AE) calculations, illustrated in the graph, indicate that an optimal density of 7.0% provides the highest selectivity compared to other densities for five wavelengths. (f) The absorption of the red type is represented, considering the fabrication process involving a GaAs substrate and a transparent polymer, with a density of 7.0%.

3.3. Optimal pattern for photon-selective absorption

As mentioned above, perfectly crystallized patterns are disadvantageous in spatial tolerance when specific distance conditions are proposed. In addition, randomly distributed components mutually affect each other and cause the degradation of selectivity. To find the optimum pattern, we create three types of point pattern and implement the numerical statistics to compare optical performances. Figure 4(a) depicts the generated arrays of regular, multi-HUD, and random points pattern where each type of nanowires is uniformly dispersed in a quantity of five. To reflect the spatial efficiency, parameters such as the diameter, height, and density of NWAs are identical in all cases. Therefore, the unit domain of regular pattern consists of six cone cells with a period (P) of 0.3657 μm and area of 0.8024 μm^2 to possess the same density as the multi-HUD arrangement (i.e., 7.0%). The boundary condition for the regular point pattern is set to be periodic, assuming infinite repetition of the structure on the xy-plane. The multi-HUD arrangement ensures a minimum distance between each component, whereas random points have no specific distance condition. As illustrated in Fig. 4(a), the total domain of the multi-HUD arrangement is 2.7 times the unit domain in the x-direction and 1.8 times the unit domain in the *y*-direction for a regular arrangement. Through this calculation, the number of each cell type in the regular arrangement is 4.86, which is lower than the numbers in a multi-HUD arrangement.

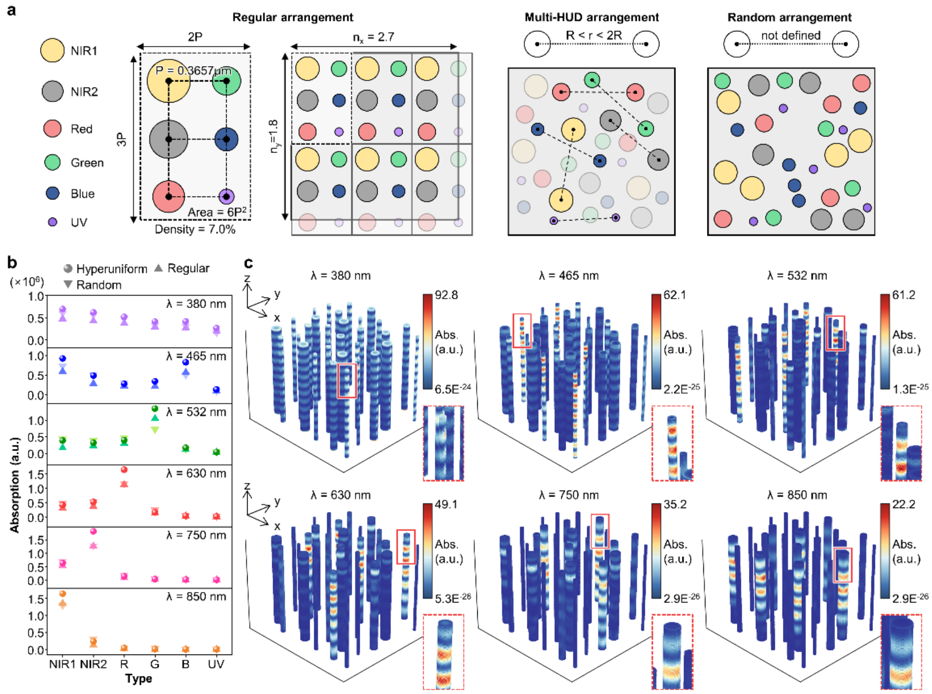

Fig. 4. The outstanding selectivity of the multi-HUD arrangement compared to regular and random patterns. (a) Three types of arrangement and the calculation method of the total segments for a regular array. Random and multi-HUD arrangement of nanowires within the area of 2×2 μm^2. To cover the total area with regularly arranged patterns, we need to multiply the number of segments in each transverse and longitudinal direction that can be positioned. (b) Absorption at each wavelength (i.e., 850, 750, 630, 532, 465, and 380 nm) by type (i.e., NIR1, NIR2, R, G, B, and UV) is compared for HUD, regular, and random structures. The HUD arrangement exhibits higher wavelength selectivity compared to the other patterns. (c) Three-dimensional absorption profiles are constructed by stacking 2D profiles along the *z*-axis, using a grid size of 10 nm for each wavelength. The cropped images highlight significant absorption at the corresponding wavelengths within the NWA.

Based on accumulated values of the absorptivity across the *z*-axis, we can calculate the selectivity according to six wavelengths as shown in Fig. 4(b). Owing to the spatial limitations as mentioned above, the regular arrangement considers four NWs for each type, while the random and multi-HUD arrangement consist of five NWs for each type. At a standard density of 7.0%, the multi-HUD NWAs exhibit the highest selective absorption ranging from UV to NIR. Furthermore, the multi-HUD configuration demonstrates notable absorption at 850 nm even though GaAs has a bandgap corresponding to 873 nm. This result can be explained by the NWA structure, which can induce slow light, thereby increasing light-matter interaction despite the low extinction coefficient of GaAs at 850 nm [49–51]. To prove the outstanding performance of the optimum HUD pattern, we construct three-dimensional absorption profiles by stacking the 2D profiles along the *z*-axis, with a grid size of 10 nm (Fig. 4(c)). As the wavelength increases to 850 nm, the contrast in absorption becomes stronger since NWs with larger diameters can absorb the subwavelength structure. The significant absorption for corresponding wavelengths in the NWA can be observed from the cropped images. At 380 nm, the low sensitivity occurs because the high absorption coefficient of GaAs causes larger NWs to absorb more UV light. As presented in Section 2 of Supplement 1, when the extinction coefficient (κ) decreases from 2.24 (i.e., the extinction coefficient of GaAs) to 1, the calculated absorption efficiency increases. To apply UV light in image sensors, material with a low extinction coefficient is preferable.

Furthermore, evaluating the applicability of the optimized multi-HUD system in multi-spectral imaging is proposed by calculating photocurrent. The photocurrent can be obtained from the absorptance of the multi-HUD system and quantum efficiency (QE) of GaAs as expressed in the following Eq. (3) [52]:

$$I_{ph} = QE \times \frac{P_{opt} \times \lambda}{h \times c} \times e \times \varepsilon \tag{3}$$

where, P_{opt} represents the incident optical power, λ is the wavelength, h is Planck's constant, c is the velocity of light, e is the elementary charge, and ε is the absorptance of the multi-HUD structure. In Section 3 of Supplement 1, the absorptance of the multi-HUD system, the QE of GaAs, and the calculated photocurrent spectrum are presented. The absorptance of the multi-HUD system is highly selective at wavelengths corresponding to NIR1 (850 nm), NIR2 (750 nm), R (630 nm), G (532 nm), and B (465 nm). Additionally, the QE of GaAs is significantly high in the wavelength range from 400 nm to 900 nm [53]. Consequently, the photocurrent derived from the product of QE and absorptance, is also elevated at these wavelengths, making them suitable for validating multi-spectral imaging detection. As shown in Fig. 5, an original image composed of RGB components for the visible range and grayscale components for the NIR range is generated to enable multi-spectral imaging. Since NIR wavelengths are difficult to represent using RGB components, thereby grayscale is utilized. By multiplying the original image by the calculated photocurrent, we derived intensity values that indicate the detection

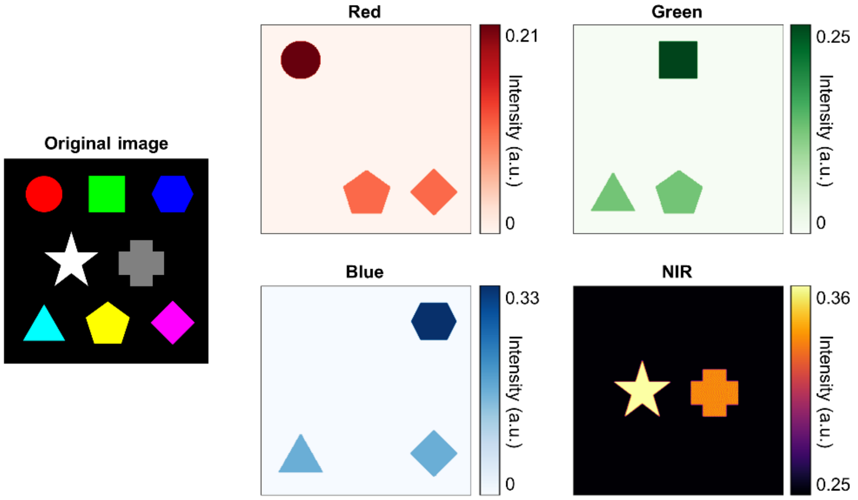

Fig. 5. An original image and intensity values for multi-spectral imaging. An original image is generated for validating multi-spectral imaging. In the NIR range, a white star represents the wavelength of 850 nm (NIR1), and a gray cross shape indicates the wavelength of 750 nm (NIR2). The shapes corresponding to each wavelength in the visible range are as follows: a red circle for 630 nm, a green square for 532 nm, and a blue hexagon for 465 nm. Additionally, a cyan triangle represents a mixture of green and blue, a yellow pentagon depicts a combination of red and green components, while a magenta diamond shape indicates a mixture of red and blue components. The intensity results of the RGB components for the visible range and the grayscale component for the NIR region exhibit high selectivity for image detection in multi-spectral imaging.

degree for each RGB component in the visible range and for the grayscale component in the NIR range, as shown in Fig. 5. For the intensity values of the red component, only the red circle, yellow pentagon, and magenta diamond shapes are exhibited with varying intensity levels. The intensity values of the green component are only visible in the green square, cyan triangle, and yellow pentagon, while the intensity values of blue component are shown in the blue hexagon, cyan triangle, and magenta diamond. Additionally, for the NIR, two shapes that are represented by grayscale in the original image are displayed with different intensity values, indicating that the star shape corresponds to NIR1 and the cross shape to NIR2. In conclusion, our multi-HUD system demonstrates high selectivity for image detection in multi-spectral imaging.

3.4. Silicon-based multi-hyperuniform photoreceptors

Similar to GaAs, silicon has desirable optical constants in the visible region (Section 4 of Supplement 1). Moreover, silicon offers significant advantages in terms of cost-effectiveness and ease of fabrication for its abundant availability. Therefore, silicon is highly suitable for large-scale production and integration into a wide range of optoelectronics. To evaluate the optical efficiency of silicon multi-HUD NWA, we carry out the numerical analysis using the identical process as for GaAs. Six wavelengths are selected to optimize the diameter of a silicon nanowire: 400 nm, 450 nm, 500 nm, 550 nm, 600 nm, and 650 nm. Through the result of Fig. 6(a), corresponding

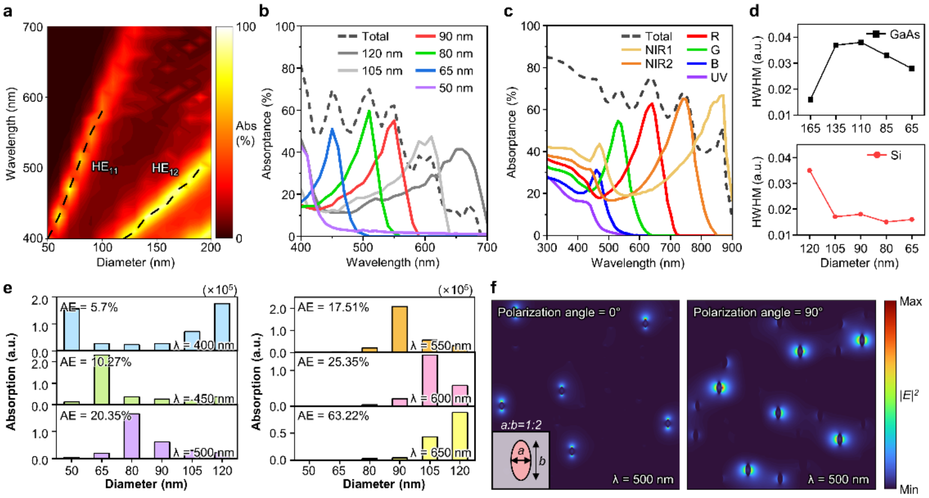

Fig. 6. The photon-absorption selectivity of the multi-HUD silicon NWA and its polarization-recognizable ability. (a) At a period of 800 nm, we can observe that the HE$_{11}$ mode of a silicon nanowire is distinguishable from other modes across the visible region. The diameters of the Si NWs are set to 50, 65, 80, 90, 105, and 120 nm, which correspond to wavelengths of 400, 450, 500, 550, 600, and 650 nm, respectively. (b) The absorptance results of the total and each type. At corresponding wavelengths, individual types show narrow-selective absorption peaks and follow the absorption pattern of all types. (c) The absorptance results of GaAs. The absorptance spectra is calculated from reflected and transmitted power, which demonstrates that GaAs has outstanding selective-absorption performance with highly narrow absorption peaks. (d) The HWHM values for GaAs and Si show that Si has a narrower HWHM than GaAs across almost all types. (e) The AE for each type ranges from 5.7% to 63.22%, which is calculated through statistical analysis. (f) 2D profiles for electric field at polarization angles of 0° and 90°. When the polarization angle is 0° (i.e., TM mode), nanowires with a major radius of 64 nm react with the light source. On the other hand, nanowires with a minor radius of 92 nm primarily respond to 90°-polarized light (i.e., TE mode).

diameters for each wavelength are set to 50 nm, 65 nm, 80 nm, 90 nm, 105 nm, and 120 nm, respectively. We compose the silicon NWA with a 5.5% dense array, in which the number of each cell type is six. The absorptance in the entire and each cell type of Si NWA derives from the power calculation (Fig. 6(b)). The absorptance (A) spectra is calculated from reflectance (R) and transmittance (T). Each individual type maintains the sensitivity of 40%, and the absorptance of each type of NW follows the total quantity at their respective wavelengths. Since the proportion of NWs with large diameters is increased in the single type, the absorptance enhancement of single type NWs occurs at longer wavelengths compared to the total type. Additionally, Fig. 6(c) exhibits the absorptance spectra for various types of GaAs NWA, calculated using the same method applied to Si NWA. The absorptance spectra indicate that GaAs exhibits significant selective absorption performance, characterized by highly narrow absorption peaks. To highlight the selective absorption capability of Si, we calculate the HWHM values from the absorptance results of Si and GaAs (Fig. 6(d)). The HWHM derives from the right half of the maximum, indicating the width of the absorption peak at half its maximum value on the right side. Si NWA displays a lower HWHM than GaAs NWA with, an average HWHM of 0.0202 compared to 0.0304 for GaAs NWA. Consequently, enhanced optical performance (i.e., photon-sensitivity and wavelength selectivity) can be achieved through Si NWA especially in the color region. Furthermore, the spatial sampling capability assesses the selectivity of silicon NWs. Figure 6(e) exhibits the AE of each type at corresponding wavelengths. The Si NWA demonstrates the highly sensitive response like the results in GaAs NWA. Along the wavelength, the AE varies from 5.7% to 63.22% because the larger nanowires at specific wavelengths can absorb subwavelength incidence.

Moreover, we construct elliptical Si NWA to analyze polarization recognition efficiency in the HUD system, as depicted in Fig. 6(f). The aspect ratio of the ellipse is set to 1:2 for the minor to major axis, with the area being the same as circular nanowires. Elliptical Si NWA can absorb each polarization mode according to the axis direction and radius length [54]. Figure 6(f) displays electric field profiles at polarization angles of 0° (TM mode) and 90° (TE mode). The wavelength of light source is 500 nm. When the plane of incidence is the *yz*-plane, the TM mode is sensitive to the major axis while the TE mode responds to the minor axis. The responsible types of the nanowire are also distinct in each case due to the difference in the ellipse radius for two axes. Therefore, the elliptical Si HUD system possesses the advantages of both selective absorption and polarization-resolving ability.

4. Conclusion

In this work, we optically optimize the nanowire-based artificial retinas to be sensitive and wavelength-selective. The diameter of GaAs NWs varies within the nanoscale to achieve a fundamental mode-dominant state at corresponding wavelengths. Additionally, an appropriately dense array (i.e., 7.0%) enables improved spectral-filtering efficiency. In comparison to regular and random configurations, the HUD system demonstrates the highest spectral selectivity with respect to the total number of locatable segments. To consider the fabrication process of NWA, we introduce diverse cases where GaAs HUD is arranged without a substrate, with a GaAs substrate, and covered with PDMS layer. Therefore, this correlated disorder system provides significantly enhanced absorption in a narrow spectral range and consequently benefits device compactness. We also validate our multi-HUD system exhibits high selectivity in image detection for multi-spectral imaging. Additionally, Si HUD configuration shows the outstanding selectivity in the visible region. By calculating the absorption from each type to total type, we can observe the spectral sampling performances of the Si HUD system. Though the HUD structure is addressed for GaAs and Si in this study, the nanowire-based HUD system can be extended to various inorganic materials such as ZnO, TiO_2, and perovskite [55,56]. In conclusion, these advanced features can address the primary hurdle in the visual functions of current optoelectronics, robotics, and unmanned vehicles.

Funding. Pusan National University; National Research Foundation of Korea.

Acknowledgments. This work was supported by 'Regional innovation mega project' program through the Korea Innovation Foundation funded by Ministry of Science and ICT (grant no. 2023-DD-UP-0015). This work was supported by the National Research Foundation of Korea (NRF) grant funded by the Korea government (MSIT) (No. RS-2024-00349776, Development of a Fully Bio-inspired Imaging System with High-Density Pixels and Neural Synapse Features Based on Single-Lens and Curved Image Sensor). This work was also supported by 2024 BK21 FOUR Graduate School Innovation Support funded by Pusan National University (PNU-Fellowship program).

Disclosures. The authors declare no conflicts of interest.

Data availability. Data underlying the results presented in this paper are not publicly available at this time but may be obtained from the authors upon reasonable request.

Supplemental document. See Supplement 1 for supporting content.

References

1. G. J. Lee, C. Choi, D. Kim, *et al.*, "Bioinspired Artificial Eyes: Optic Components, Digital Cameras, and Visual Prostheses," Adv. Funct. Mater. **28**(24), 1705202 (2018).
2. D. H. Kim, J. J. Kim, D.-J. Kong, *et al.*, "Bio-inspired tunable optics and photonics: bridging the gap between nature and technology," International J. Optomechatronics **18**(1), 5 (2024).
3. Won Bae Han, S. Heo, D. Kim, *et al.*, "Zebra-inspired stretchable, biodegradable radiation modulator for all-day sustainable energy harvesters," Sci. Adv. **9**(5), eadf5883 (2023).
4. P. López-Osorio, J. P. Domínguez-Morales, and F. Perez-Peña, "A Neuromorphic Vision and Feedback Sensor Fusion Based on Spiking Neural Networks for Real-Time Robot Adaption," Advanced Intelligent Systems **6**(5), 2300646 (2024).
5. O. Villi and M. Yakar, "Sensor technologies in unmanned aerial vehicles: types and applications," Advanced UAV **4**(1), 1–18 (2024).
6. M. Kim, G. J. Lee, C. Choi, *et al.*, "An aquatic-vision-inspired camera based on a monocentric lens and a silicon nanorod photodiode array," Nat. Electron. **3**(9), 546–553 (2020).
7. M. Lee, G. J. Lee, H. J. Jang, *et al.*, "An amphibious artificial vision system with a panoramic visual field," Nat. Electron. **5**(7), 452–459 (2022).
8. M. Kim, S. Chang, M. Kim, *et al.*, "Cuttlefish eye–inspired artificial vision for high-quality imaging under uneven illumination conditions," Science Robotics **8**(75), eade4698 (2023).
9. J. Park, M. S. Kim, J. Kim, *et al.*, "Avian eye–inspired perovskite artificial vision system for foveated and multispectral imaging," Science Robotics **9**(90), eadk6903 (2024).
10. M. Sung Kim, M. S. Kim, G. J. Lee, *et al.*, "Bio-Inspired Artificial Vision and Neuromorphic Image Processing Devices," Adv. Mater. Technol. **7**(2), 2100144 (2022).
11. W. Gao, Z. Xu, X. Han, *et al.*, "Recent advances in curved image sensor arrays for bioinspired vision system," Nano Today **42**, 101366 (2022).
12. C. Choi, M. K. Choi, S. Liu, *et al.*, "Human eye-inspired soft optoelectronic device using high-density MoS2-graphene curved image sensor array," Nat. Commun. **8**(1), 1664 (2017).
13. M. S. Kim, J.-E. Yeo, H. Choi, *et al.*, "Evolution of natural eyes and biomimetic imaging devices for effective image acquisition," J. Mater. Chem. C **11**(36), 12083–12104 (2023).
14. S. Kim, J. J. Cassidy, B. Yang, *et al.*, "Hexagonal Patterning of the Insect Compound Eye: Facet Area Variation, Defects, and Disorder," Biophys. J. **111**(12), 2735–2746 (2016).
15. P. A. Raymond, S. M. Colvin, Z. Jabeen, *et al.*, "Patterning the Cone Mosaic Array in Zebrafish Retina Requires Specification of Ultraviolet-Sensitive Cones," PLOS ONE **9**(1), e85325 (2014).
16. T. W. Cronin, M. J. Bok, N. J. Marshall, *et al.*, "Filtering and polychromatic vision in mantis shrimps: themes in visible and ultraviolet vision," Phil. Trans. R. Soc. B **369**(1636), 20130032 (2014).
17. K. M. Jenkins, D. E. G. Briggs, and J. Luque, "The remarkable visual system of a Cretaceous crab," iScience **25**(1), 103579 (2022).
18. J. Luque, W. T. Allison, H. D. Bracken-Grissom, *et al.*, "Evolution of crab eye structures and the utility of ommatidia morphology in resolving phylogeny," BioRxiv, 786087 (2019).
19. L. M. Joan and Roach, "Junctional structures in the crystalline cone of the crayfish compound eye," Cell Tissue Res. **173**(3), 309 (1976).
20. J. G. Kim, S. H. Kim, J. Y. Park, *et al.*, "Correlation between Feeding Behaviors and Retinal Photoreceptor Cells of Largemouth Bass, Micropterus salmoides, in Korea," Fishes **7**(1), 25 (2022).
21. A. S. French, A. W. Snyder, and D. G. Stavenga, "Image degradation by an irregular retinal mosaic," Biological Cybernetics **27**(4), 229–233 (1977).
22. D. K. Lubensky, M. W. Pennington, B. I. Shraiman, *et al.*, "A dynamical model of ommatidial crystal formation," Proc. Natl. Acad. Sci. U. S. A. **108**(27), 11145–11150 (2011).

23. M. M. Milošević, W. Man, G. Nahal, *et al.*, "Hyperuniform disordered waveguides and devices for near infrared silicon photonics," Sci. Rep. **9**(1), 20338 (2019).
24. W. Man, M. Florescu, E. P. Williamson, *et al.*, "Isotropic band gaps and freeform waveguides observed in hyperuniform disordered photonic solids," Proc. Natl. Acad. Sci. U. S. A. **110**(40), 15886–15891 (2013).
25. M. M. Milosevic, M. Florescu, W. Man, *et al.*, "Hyperuniform disordered photonic band gap devices for silicon photonics," *11th International Conference on Group IV Photonics* (IEEE, 2014).
26. C. Tedore and D.-E. Nilsson, "Avian UV vision enhances leaf surface contrasts in forest environments," Nat. Commun. **10**(1), 238 (2019).
27. A. Bringmann, "Structure and function of the bird fovea," Anatomia, Histologia, Embryologia **48**(3), 177–200 (2019).
28. I. C. Cuthill, J. C. Partridge, A. T. D. Bennett, *et al.*, "Ultraviolet Vision in Birds," *Advances in the Study of Behavior* (Academic Press, 2000).
29. M. P. Jones, K. E. Pierce, and D. Ward, "Avian Vision: A Review of Form and Function with Special Consideration to Birds of Prey," J. Exotic Pet Medicine **16**(2), 69–87 (2007).
30. J. K. Bowmaker, L. A. Heath, S. E. Wilkie, *et al.*, "Visual pigments and oil droplets from six classes of photoreceptor in the retinas of birds," Vision Res. **37**(16), 2183–2194 (1997).
31. T. Baden and D. Osorio, "The Retinal Basis of Vertebrate Color Vision," Annu. Rev. Vis. Sci. **5**(1), 177–200 (2019).
32. D. Wilby, M. B. Toomey, P. Olsson, *et al.*, "Optics of cone photoreceptors in the chicken (*Gallus gallus domesticus*)," J. R. Soc. Interface. **12**(111), 20150591 (2015).
33. B. Vohnsen, "Directional sensitivity of the retina: A layered scattering model of outer-segment photoreceptor pigments," Biomed. Opt. Express **5**(5), 1569 (2014).
34. M. J. Piket-May, J. B. Troy, and A. Taflove, "Electrodynamics of visible-light interactions with the vertebrate retinal rod," Opt. Lett. **18**(8), 568 (1993).
35. V. B. Morris, "Symmetry in a receptor mosaic demonstrated in the chick from the frequencies, spacing and arrangement of the types of retinal receptor," J. Comp. Neurol. **140**(3), 359–397 (1970).
36. H. Orestis Christogeorgos, Q. Zhang, Cheng, *et al.*, "Extraordinary Directive Emission and Scanning from an Array of Radiation Sources with Hyperuniform Disorder," Phys. Rev. Applied **15**(1), 014062 (2021).
37. H. Zhang, W. Wu, Q. Cheng, *et al.*, "Reconfigurable Reflectarray Antenna Based on Hyperuniform Disordered Distribution," IEEE Trans. Antennas Propag. **70**(9), 7513–7523 (2022).
38. Y. Jiao, T. Lau, H. Hatzikirou, *et al.*, "Avian photoreceptor patterns represent a disordered hyperuniform solution to a multiscale packing problem," Phys. Rev. E **89**(2), 022721 (2014).
39. K. Tang, Y. Wang, S. Wang, *et al.*, "Hyperuniform Disordered Parametric Loudspeaker Array," Phys. Rev. Appl. **19**(5), 054035 (2023).
40. D. Wan, T. Li, S. Chen, *et al.*, "Hyperuniform Disordered Solids with Morphology Engineering," Laser Photonics Rev. **17**(11), 2300398 (2023).
41. Y. A. Kram, S. Mantey, and J. C. Corbo, "Avian Cone Photoreceptors Tile the Retina as Five Independent, Self-Organizing Mosaics," PLoS ONE **5**(2), e8992 (2010).
42. D.-M. Geum, S. Kim, S. K. Kim, *et al.*, "Monolithic integration of visible GaAs and near-infrared InGaAs for multicolor photodetectors by using high-throughput epitaxial lift-off toward high-resolution imaging systems," Sci. Rep. **9**(1), 18661 (2019).
43. A. M. Hoang, A. Dehzangi, S. Adhikary, *et al.*, "High performance bias-selectable three-color Short-wave/Mid-wave/Long-wave Infrared Photodetectors based on Type-II InAs/GaSb/AlSb superlattices," Sci. Rep. **6**(1), 24144 (2016).
44. G. J. Lee, K. Park, M. S. Kim, *et al.*, "Selective and Sensitive Photon Sieve Based on III–V Semiconductor Nanowire Forest Fabricated by Lithography-Free Process," Adv. Opt. Mater. **8**(17), 2000198 (2020).
45. K. M. Azizur-Rahman and R. R. LaPierre, "Wavelength-selective absorptance in GaAs, InP and InAs nanowire arrays," Nanotechnology **26**(29), 295202 (2015).
46. G. Saerens, E. Bloch, K. Frizyuk, *et al.*, "Second-harmonic generation tuning by stretching arrays of GaAs nanowires," Nanoscale **14**(24), 8858–8864 (2022).
47. J. Walia, N. Dhindsa, J. Flannery, *et al.*, "Diameter dependent heating in GaAs nanowires," *14th International Conference on Nanotechnology* 893–895 (IEEE, 2014).
48. T. Baba, "Slow light in photonic crystals," Nat. Photonics **2**(8), 465–473 (2008).
49. S. A. Schulz, J. Upham, Liam, *et al.*, "Photonic crystal slow light waveguides in a kagome lattice," Opt. Lett. **42**(16), 3243 (2017).
50. J. Grgić, S. Xiao, J. Mørk, *et al.*, "Slow-light enhanced absorption in a hollow-core fiber," Opt. Express **18**(13), 14270 (2010).
51. H. Park and K. B. Crozier, "Elliptical silicon nanowire photodetectors for polarization-resolved imaging," Opt. Express **23**(6), 7209 (2015).
52. K. Ramakrishnan, B. Ajitha, and Y. Ashok, "Review on metal sulfide-based nanostructures for photodetectors: From ultraviolet to infrared regions," Sensors and Actuators A: Physical **349**, 114051 (2023).
53. N. Mohammad, P. Wang, D. J. Friedman, *et al.*, "Enhancing photovoltaic output power by 3-band spectrum-splitting and concentration using a diffractive micro-optic," Opt. Express **22**(S6), A1519 (2014).
54. Y.-Z. Long, M. Yu, B. Sun, *et al.*, "Recent advances in large-scale assembly of semiconducting inorganic nanowires and nanofibers for electronics, sensors and photovoltaics," Chem. Soc. Rev. **41**(12), 4560 (2012).

55. D. Zhang, Y. Zhu, Q. Zhang, *et al.*, "Vertical Heterogeneous Integration of Metal Halide Perovskite Quantum-Wires/Nanowires for Flexible Narrowband Photodetectors," Nano Lett. **22**(7), 3062–3070 (2022).
56. R. Bridson, "Fast Poisson disk sampling in arbitrary dimensions," ACM SIGGRAPH 2007 Sketches on - SIGGRAPH **07**, 22 (2007).